

Anisotropy of optical phonons and interface modes in GaAs-AlAs superlattices

Shang-Fen Ren, Hanyou Chu, and Yia-Chung Chang

*Department of Physics and Materials Research Laboratory, University of Illinois at Urbana-Champaign,
1110 West Green Street, Urbana, Illinois 61801*

(Received 16 November 1987)

In this paper phonon properties of GaAs-AlAs superlattices are studied with an 11-parameter rigid-ion model. Short-range interactions up to the second neighbors are included, and the long-range Coulomb interaction is calculated exactly. Modes propagating both normally ($k_{\parallel}=0$) and obliquely ($k_{\parallel}\neq 0$) to the interfaces are studied for a number of GaAs-AlAs superlattices. Anisotropy of zone-center optical phonons is examined in detail. Phonon dispersion relations of large-size GaAs-AlAs superlattices are calculated and many interface modes are identified. All results are compared with the existing experimental data with favorable agreement.

I. INTRODUCTION

In the last decade, semiconductor superlattices have attracted much attention from scientists in both theoretical and experimental areas, because of potential applications in semiconductor devices. Compared to the electronic properties, lattice-vibrational properties of superlattices have been much less studied.¹ Most experimental information on superlattice phonons is obtained from Raman scattering measurements, which probe the phonon modes with wave vectors near the center of the Brillouin zone.²⁻⁷ Several theoretical models have been developed to study the phonons in superlattice systems. The linear-chain model has been used⁵ to analyze phonon modes with wave vectors perpendicular to the interfaces. It gives results in reasonable agreement with experiments, but cannot be used to analyze phonon modes with wave vectors parallel to the interfaces. The dielectric continuum model was used to explain the interface and slab modes and the anisotropy of optical phonons⁷⁻¹² from a macroscopic point of view. Yip and Chang¹³ reported calculations in an adiabatic bond-charge model which includes the Coulomb interaction by a perturbational method. Kobayashi¹⁴ performed calculations in a rigid-ion model, with wave vectors both perpendicular and parallel to the interfaces, but with the long-range Coulomb interaction completely ignored. Toriyama *et al.*¹⁵ calculated phonons in a (1,1) GaAs-AlAs superlattice, using a rigid-ion model with Coulomb interaction. All the above microscopic calculations did not address questions regarding the anisotropy of zone-center optical-phonon modes and the interface modes which have been observed experimentally. Apparently, more thorough theoretical studies based on a microscopic model which takes into account the Coulomb interaction are needed. Here we are trying to provide such theoretical studies by using an 11-parameter rigid-ion model.^{16,17} A brief account of this work was previously reported in Ref. 18.

In Sec. II, we briefly review the 11-parameter rigid-ion model which gives reasonably accurate phonon dispersion curves of III-V semiconductors, and we explain how

we adapt this model to the study of superlattices. In Sec. III, we present results for phonon dispersion curves of GaAs-AlAs superlattices along the growth ([001]) and in-plane ([100] and [110]) directions. The angular dependence of the zone-center optical modes will be discussed. The displacement vectors are also calculated to improve the understanding of the anisotropy of optical modes. In Sec. IV, the phonon dispersion relations of large-period GaAs-AlAs superlattices are calculated and interface modes are identified by comparing the superlattice phonon bands with the bulk phonon bands of GaAs and AlAs. Section V summarizes our results.

II. 11-PARAMETER RIGID-ION MODEL AND APPLICATION TO SUPERLATTICES

The rigid-ion model has been used extensively to describe the interactions between atoms in crystals.¹⁹ In this model, the polarization in an ionic crystal is determined completely by the displacements of ions (assumed pointlike) from their equilibrium positions, and the interactions between atoms are divided into two parts, the short-range interaction and the long-range Coulomb interaction. The 11-parameter rigid-ion model developed by Kunc *et al.*,^{17,18} which we shall adopt for superlattices, has been used to calculate the phonon dispersion curves of many III-V semiconductors successfully.

In the 11-parameter rigid-ion model, only the nearest and second-neighbor forces are included in the short-range part. Of the 11 parameters, two parameters are used to describe the interactions between the nearest-neighbor cation-anion interactions, four parameters are used to describe the second-neighbor cation-cation interactions, another four parameters are used to describe the second-neighbor anion-anion interactions, and the last parameter Q , the electron transfer charge, is used to describe the strength of the long-range Coulomb interactions between the ions.

To study the phonon dispersion relation, we solve the equation of motion for ions,

$$\omega^2(\mathbf{k})\underline{M}\mathbf{U} = \underline{C}(\mathbf{k})\mathbf{U}, \quad (1)$$

where \underline{M} is the mass matrix and $\underline{C}(\mathbf{k})$ is the dynamic matrix which consists of two parts—the short-range (SR) interaction matrix and the Coulomb (C) interaction matrix:

$$\underline{C}(\mathbf{k}) = \underline{C}^{\text{SR}}(\mathbf{k}) + \underline{C}^C(\mathbf{k}). \quad (2)$$

For convenience of later discussion, we define an atomic layer as a collection of atoms in a plane normal to the growth direction, a bilayer as two adjacent atomic layers, and a sublattice as a collection of all equivalent atomic layers (one in each period) of the superlattice. In an (m, n) GaAs-AlAs superlattice, each period is composed of m bilayers of GaAs and n bilayers of AlAs, and the whole system is composed of $2(m+n)$ sublattices. We shall use the label J for the bilayers in a given period and (J, σ) for the two atomic layers associated with bilayer J ; $\sigma=1$ for cation layers and 2 for anion layers. Similarly, sublattices are labeled by (J, σ) .

In adapting the 11-parameter rigid-ion model to the superlattice, we choose the short-range interaction parameters between any two atoms in the superlattice to be the same as those in the corresponding bulk material with the exception that the interaction between a Ga atom and an Al atom across an interface is taken to be the average of the Ga-Ga interaction in bulk GaAs and the Al-Al interaction in bulk AlAs. We also performed some calculations in which we averaged the interaction parameters for atoms near the interface over a few neighboring layers, but no qualitative differences were found.

The parameters of GaAs we used are taken from Kunc.¹⁷ Because of the uncertainty in AlAs phonon dispersion curves, we consider two sets of interaction parameters for AlAs: one is fitted to the existing experimental data^{3,5,20} and the other is fitted to the theoretical calculation of Yip and Chang.¹³ The parameters used in our calculation are listed in Table I. Figure 1 shows the calculated dispersion curves of AlAs based on the two sets of parameters of Table I. The experimental data are also shown as dark circles for comparison. Only the results obtained by using the first set of parameters are presented in this paper, since the results obtained by using the second set of parameters are qualitatively similar.

The large splitting of the longitudinal- and transverse-optical modes at the zone center indicates that the long-range Coulomb interaction cannot be neglected in III-V semiconductors and superlattices. The fundamental theory on how to include the long-range Coulomb interaction in the rigid-ion model was discussed in detail by Born and Huang,¹⁹ Maradudin,²¹ and by Venkataraman²² *et al.* The connection between the macroscopic and microscopic theories for bulk crystals was also established.^{19,21,22} However, it is more difficult to treat the long-range Coulomb interaction in the superlattice be-

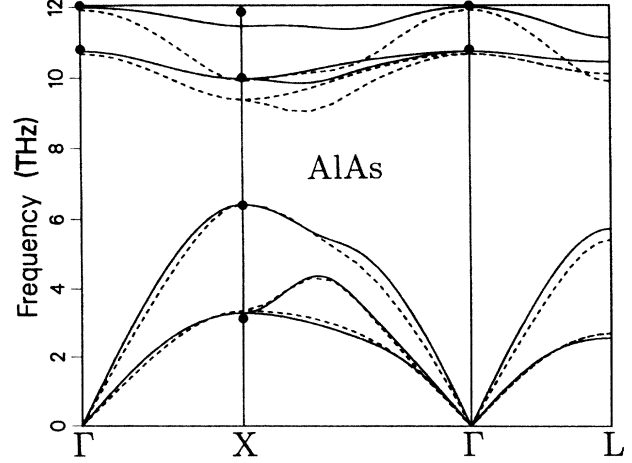


FIG. 1. The dispersion curves of bulk AlAs calculated by using 11-parameter rigid-ion model. The solid curves are the results of parameters fitted to the existing experimental data, and the dashed curves are the results of parameters fitted to the theoretical calculation of Yip and Chang (Ref. 13).

cause of its lower symmetry. The Ewald transformation which ensures fast convergence for evaluating the Coulomb interaction in bulk crystals must be modified for superlattices. We have generalized the Ewald transformation method to calculate the Coulomb matrix elements between any two atomic layers. For two atomic layers separated by a finite distance, our method is closely related to that of Yip and Chang.¹³ However, we have rederived the formulas in a more straightforward way and performed the sum over all atomic layers in a sublattice. Unlike the method adopted by Yip and Chang,¹³ no truncation of the Coulomb interaction between atomic layers is made in the present calculation. This is of particular importance for getting the correct anisotropic behavior of the superlattice phonons. Details for calculating Coulomb matrix elements for superlattices are presented in the Appendix. We find that the Coulomb interaction between a sublattice $(0,0)$ and another sublattice (J, σ) as $\mathbf{k} \rightarrow 0$ can be written as

$$C_{i,j}^C(\mathbf{k}, J, \mathbf{r}_\sigma) = \left[\frac{Q_0 Q_\sigma 4\pi}{vN} \right] \frac{k_i k_j}{k^2} + D_{i,j}(J, \mathbf{r}_\sigma) \quad (3)$$

where i, j indicate the x, y, z directions, Q_0 and Q_σ represent the atomic transfer charges of atoms in sublattice $(0,0)$ and sublattice (J, σ) , respectively, v is the volume of the bulk unit cell, $\mathbf{r}_\sigma = (0, 0, 0)$, $(1, 1, 1)a/4$ for $\sigma = 1, 2$, and N is the total number of bilayers in a period.

TABLE I. Interaction parameters of AlAs in the rigid-ion model. The first set of parameters is fitted to the existing experimental data, and the second set of parameters is fitted to the theoretical calculation of Yip and Chang (Ref. 13). The units of these parameters are the same as those defined in Ref. 17.

	A	B	C_1	D_1	E_1	F_1	C_2	D_2	E_2	F_2	Q
I	-0.4083	-0.0806	-0.0359	0.0112	0.0394	0.0115	-0.0169	-0.1007	-0.0349	0.1461	0.7548
II	-0.4030	-0.1262	-0.0001	0.0329	0.0259	-0.0002	-0.0190	-0.0648	0.0383	0.1393	0.7548

$N=(m+n)$ for an (m,n) GaAs-AlAs superlattice. In our calculation, the bulk GaAs electron transfer charge Q_a is used for inner GaAs layers, and the bulk AlAs electron transfer charge Q_b for inner AlAs layers. At the interfaces, the transfer charge of As is taken to be the average of Q_a and Q_b since the electron overlapping is significant only for the nearest neighbors.

The first term in the right-hand side of Eq. (3) is an irregular function, which has different values when \mathbf{k} approaches zero from different directions. The second term $D_{i,j}(J, \mathbf{r}_\sigma)$, which must be calculated numerically, is direction independent. This result is similar to that of a bulk system. However, in a bulk zinc-blende crystal, \underline{D} can be reduced to a constant multiplied by a three-dimensional identity matrix, whereas in the superlattice \underline{D} takes the following form:

$$\underline{D}(J, \mathbf{r}_\sigma) = \begin{pmatrix} a_1 & 0 & 0 \\ 0 & a_1 & 0 \\ 0 & 0 & a_2 \end{pmatrix} \quad \text{for } \sigma=1$$

and

$$\underline{D}(J, \mathbf{r}_\sigma) = \begin{pmatrix} b_1 & c & 0 \\ c & b_1 & 0 \\ 0 & 0 & b_2 \end{pmatrix} \quad \text{for } \sigma=2.$$

It can be shown that the short-range interaction between any two sublattices also has the same form. The most interesting and important conclusion one can derive from Eq. (3) is that the superlattice optical modes have different frequencies as $\mathbf{k} \rightarrow 0$ from different directions. This is due to the angular dependence of the irregular term $k_i k_j / k^2$ and the lack of rotational invariance of the matrix $\underline{D} + \underline{C}^{\text{SR}}$. For a bulk system with cubic symmetry, the matrix $\underline{D} + \underline{C}^{\text{SR}}$ is invariant under rotation. We can then choose a coordinate system in which the z axis is along \mathbf{k} , and the tensor $k_i k_j / k^2$ takes the new form

$$\begin{pmatrix} 0 & 0 & 0 \\ 0 & 0 & 0 \\ 0 & 0 & 1 \end{pmatrix}.$$

Thus, the resulting eigenfrequencies are independent of the direction of \mathbf{k} as $\mathbf{k} \rightarrow 0$.

The phenomenon of angular dependence of the optical phonon frequency in bulk materials with axial symmetry has been previously observed.^{23,24} For superlattice systems, a similar phenomenon was observed² and it was accounted for by Rytov's⁸ macroscopic theory. From the microscopic point of view, we see that it is a combined result of the long-range Coulomb interaction and the lack of cubic symmetry of the system.

From Eq. (3) it is easy to see that the anisotropy is caused by the macroscopic field from the unvanishing dipole moment. As will be explained later, lattice vibrations associated with optical branches are essentially localized in one of the two constituent materials. As far as optical modes are concerned, the superlattice behaves like an array of separated slabs coupled by the long-range Coulomb interaction. Optical modes confined in each

slab are subject to boundary conditions similar to those for an electron confined in an infinitely deep quantum well. Thus lattice vibration inside each slab can be approximately described by the displacement vectors

$$U_i(J, \sigma) = f(J) u_i^0(\sigma), \quad (4)$$

where $u_i^0(\sigma)$ is displacement vectors for the corresponding bulk optical mode of the same frequency, and $f(J)$ is a smooth "envelope" function. It was shown that in the continuum model,¹⁰ the envelope function $f(J)$ for an optical mode confined in a particular slab can be approximately described by the function $\sin[n\pi J / (N_s + \frac{1}{2})a']$ (we shall return to this point later), where N_s is the number of bilayers inside each slab, $n=1, 2, \dots, N_s$, and a' is the width of a bilayer (one half the lattice constant). Thus the total dipole moment inside each slab is approximately proportional to

$$[1 - (-1)^n] \cot \frac{n\pi}{2N_s + 1}, \quad 1 \leq n \leq N_s.$$

To get a nonvanishing macroscopic field, n has to be odd, and the $n=1$ mode (the principal mode) has the strongest dipole moment. Hence neglecting the interaction between modes with different n , there are four modes (one LO and one TO for both GaAs and AlAs slabs) which have large anisotropy. A thorough discussion of the effect of the macroscopic dipole field on the optical phonon frequencies in a uniaxial bulk system can be found in Ref. 25.

III. ANISOTROPY OF OPTICAL MODES

Phonon dispersion curves along the [001] direction for a (2,2) GaAs-AlAs superlattice are shown in Fig. 2(a). The folding of phonon dispersion curves of bulk GaAs

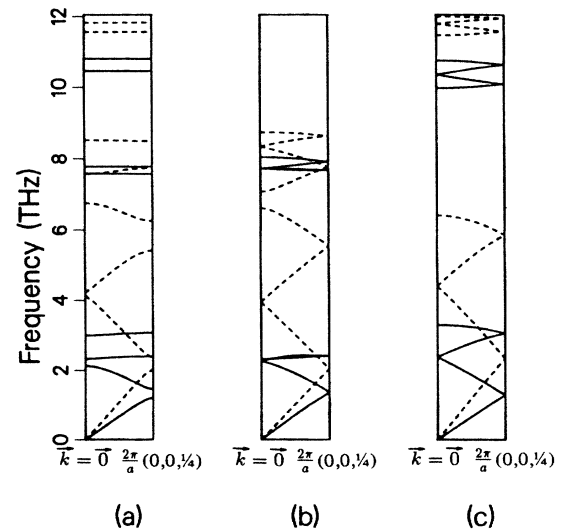


FIG. 2. (a) The dispersion curves of a (2,2) GaAs-AlAs superlattice along [001]; (b) GaAs bulk phonon dispersion curves along [001] folded over the same period as (a); (c) AlAs bulk phonon dispersion curves along [001] folded over the same period as (a). The solid curves are transverse modes (doubly degenerate) and the dashed curves are longitudinal modes.

[Fig. 2(b)] and AlAs [Fig. 2(c)] in the superlattice Brillouin zone ($\frac{1}{4}$ of the bulk Brillouin zone) are also shown for comparison. The solid curves are transverse modes (doubly degenerate) and the dashed curves are longitudinal modes. Because the optical frequencies of the bulk GaAs and AlAs have no overlap, the superlattice vibrational modes derived from bulk optical branches are either GaAs-like (confined in the GaAs slab) or AlAs-like (confined in the AlAs slab). The degree of confinement is determined by the smallest-imaginary- k solution to the corresponding bulk dynamic equation at the frequency considered. According to the calculations of Yip and Chang,¹³ the superlattice optical modes have decay lengths less than two atomic layers. Thus optical phonons are well confined even in a (2,2) superlattice. The bulk acoustical modes of GaAs and AlAs are quite similar, so the superlattice vibrational modes derived from bulk acoustical branches are mixtures of the two sets of acoustical modes. The results obtained here are in good agreement with those calculated in the adiabatic bond-charge model.¹³

Next, we discuss the phonon dispersion curves along a direction perpendicular to the growth direction (in-plane direction). Figure 3 shows the phonon dispersion curves of a (2,2) GaAs-AlAs superlattice along the [100] direction (right panel) and the [110] direction (left panel). The phonon modes with frequencies lower than 7 THz are again derived from acoustical branches. Because of the zone-folding effect, the superlattice acoustical modes contain strong mixtures of bulk TA and LA modes. As a result, we see complicated dispersion curves and several stop bands at some finite k . The stop bands of superlattice acoustical phonons for oblique incidence have recently been observed experimentally²⁶ and studied by an elastic theory.²⁷

Comparing Fig. 3 with the central panel of Fig. 2, we find that for the $n = 1$ optical modes, the frequencies are distinctly different for $k \rightarrow 0$ from the growth direction

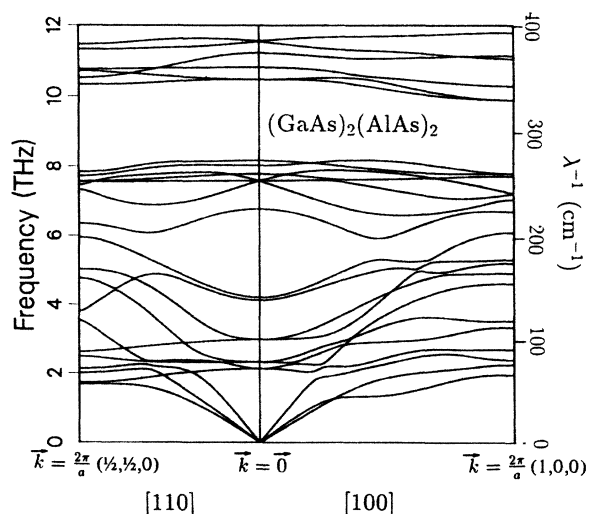


FIG. 3. Dispersion curves of (2,2) GaAs-AlAs superlattice along [110] and [100].

and from an in-plane direction. Thus, the phonon frequencies are anisotropic functions of k at $k=0$. On the other hand, we see in Fig. 3 that the phonon frequencies remain the same for k approaching zero from different in-plane directions.

In Fig. 4, we plot the frequencies of zone-center optical modes for a (2,2) GaAs-AlAs superlattice as functions of θ , the angle of the wave vector k measured from the growth direction. θ goes from 0 to $\pi/2$ as k goes from [001] to [100] in a plane normal to [010]. The solid curves are for the modes with large angular dispersion and the dashed curves are for the modes with negligible angular dispersion. The symbols LOn and TON denote the superlattice vibrational modes with principal quantum number n derived from the bulk longitudinal and transverse optical branches, respectively. There are two sets of vibrational modes labeled identically, one associated with the GaAs-like modes (lower-frequency set) and the other associated with AlAs-like modes (higher-frequency set). These labels are well defined only at $\theta=0$, since modes associated with different principal quantum numbers (n) will in general be mixed as θ deviates from zero. Because the system has a reflection symmetry with respect to a plane parallel to the interface and through the center of the GaAs or AlAs slab (hereafter referred to as the "midplane"), only modes having the same parity can be mixed. For the (2,2) superlattice, only one even mode ($n = 1$) and one odd mode ($n = 2$) are derived from each optical branch. Hence, no mixing occurs between modes of different n . However, there is still mixing between the $LO1$ and $TO1$ modes. In this figure, we see that the $n = 1$ modes have substantial angular dispersion

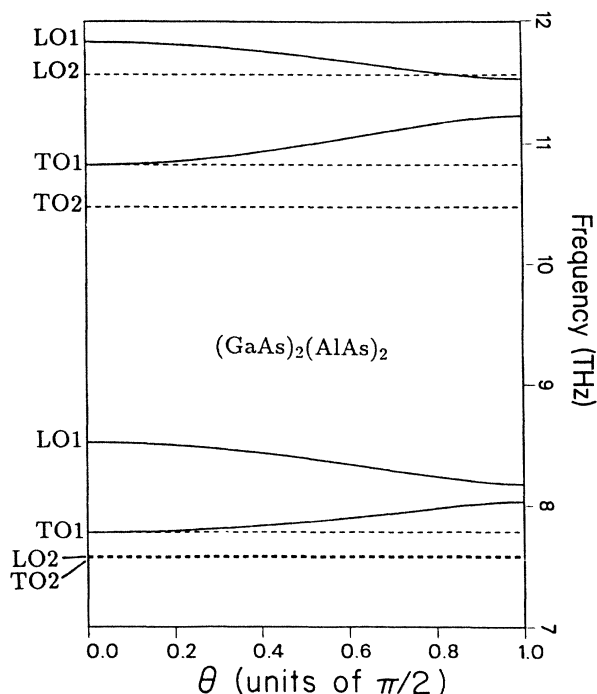


FIG. 4. Frequencies of zone-center ($k=0$) optical modes for a (2,2) GaAs-AlAs superlattice as functions of θ .

and the $n=2$ modes are dispersionless. This is consistent with the argument based on the dipole-moment consideration.

Figure 5 shows the x - and z -component vibrational strengths of the AlAs-like and GaAs-like LO1 and TO1 modes as functions of θ for a GaAs-AlAs superlattice. Here we define the vibrational strength S_i as the summation of the square of the i th component of the displacement vectors over all atomic layers within a GaAs or AlAs slab, viz.,

$$S_i = \sum_{J,\sigma} |U_i(J,\sigma)|^2.$$

We see that the AlAs-like LO1 mode [Fig. 5(a)] turns smoothly from z -like to x -like as θ goes from 0 to $\pi/2$, whereas the AlAs-like TO1 mode [Fig. 5(b)] turns smoothly from x -like to z -like, similar to the bulk LO and TO modes. There is another AlAs-like TO1 mode (not shown) which remains almost purely y -like for all values of θ and has no angular dispersion. The GaAs-like LO1 and TO1 modes [Figs. 5(c) and (d)] behave quite differently. The GaAs-like LO1 mode starts being almost purely z -like, gains some x component as θ increases and turns back to almost purely z -like at $\theta=\pi/2$, with a max-

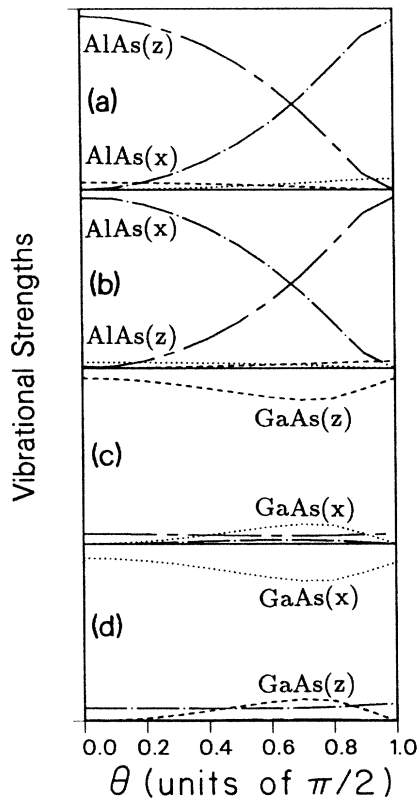


FIG. 5. x - and z -component vibrational strengths of the AlAs-like and GaAs-like LO1 and TO1 modes as functions of θ at the zone center ($\mathbf{k}=\mathbf{0}$) for a (2,2) GaAs-AlAs superlattice. (a) AlAs-like LO1, (b) AlAs-like, (c) GaAs-like LO1, and (d) GaAs-like TO1. \cdots , GaAs-like x component; $---$, GaAs-like z component; $- \cdot - \cdot -$, AlAs-like x component; $---$, AlAs-like z component.

imum x component at $\theta \approx 0.7(\pi/2)$. The GaAs TO1 mode behaves similarly, with the x and z components interchanged. The above behavior is due to the strong mixing of these two modes. In fact, at $\theta=\pi/2$, the characters of the GaAs LO1 and TO1 modes have interchanged.

Similar to Fig. 4, we show the angular dependence of frequencies as a function of θ of the (7,7) superlattices in Fig. 6. Excluding the effect of mode mixing, we see that only the $n=1$ modes can have significant angular dispersion, the other modes are essentially dispersionless. The TO1 mode splits into two branches as θ deviates from zero: only (y -like) remains dispersionless and the other (with mixed x and z components) has substantial dispersion. The $n \neq 1$ TO modes are nearly doubly degenerated for all angles. All these results can be understood by considering the dipole moments of the modes, which determine the magnitude of the angular dispersion. The dipole moment in a superlattice mode is approximately equal to the sum of dipole moments of all the bilayers in each period weighted by the superlattice envelope function. For the $n=1$ modes the envelope function is positive everywhere; thus the total dipole moment is large. For the other modes the envelope function oscillates within a period and the net dipole moment is substantially smaller. For modes derived from the acoustical branches, the dipole moments of all bilayers in each period are very small for the $n=1$ mode, which is derived from bulk acoustical modes with small wave vectors, and the net dipole moment is also small for the $n \neq 1$ modes because of the fast oscillation in the envelope function. Thus all the superlattice modes derived from acoustical branches have almost no angular dispersion.

For the $n=1$ optical modes, we cannot classify them according to the point-group irreducible representations,

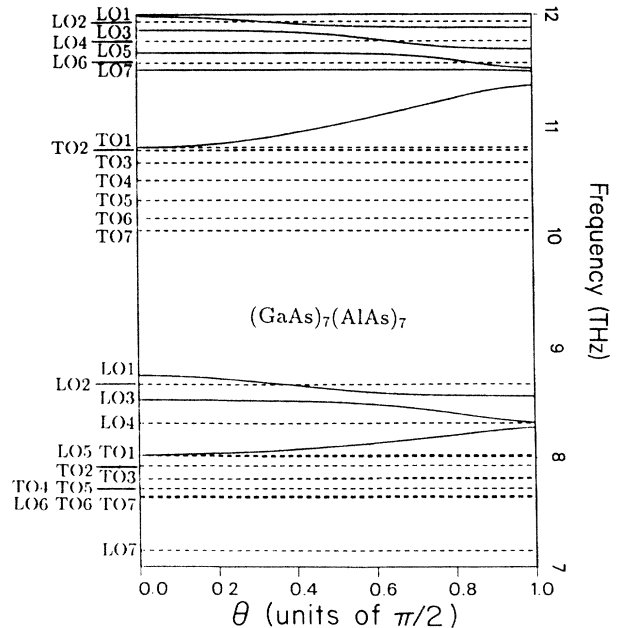


FIG. 6. Angular dependence of the optical phonons at the Brillouin zone center as a function of θ for a (7,7) GaAs-AlAs superlattice.

because their displacement vectors vary with θ . For the $n \neq 1$ modes which have negligible dipole moments, the long-range part of the Coulomb interaction can be ignored. If we only keep the short-range interactions, then the displacement vectors (the eigenvectors of the dynamic matrix) for the $\mathbf{k}=0$ modes transform according to the irreducible representations of the D_{2d} point-group. Thus for $n \neq 1$ we can classify the z -like LOn (n odd) modes as the B_2 modes, the z -like LOn (n even) modes as the A_1 modes and the x - and y -like TON modes as two degenerate E modes. In the A_1 (B_2) mode, atoms oscillate symmetrically (antisymmetrically) about the midplane in the GaAs or AlAs slab, and the corresponding envelope function is an odd (even) function about the midplane. For all superlattice modes derived from the acoustical branches, the net dipole moments are negligible; thus the LA (n odd), LA (n even), and TA modes can be similarly classified as the B_2 , A_1 , and E modes, respectively.

In Fig. 6, we see that at finite values of θ , two modes with different n mix with each other as their frequencies become close. For example, the AlAs-like LO1 mode interacts with the LO3 modes at θ near $0.4(\pi/2)$, then again interacts with the LO5 modes at θ near $0.6(\pi/2)$, and finally interacts with the LO7 modes at θ near $1.0(\pi/2)$. Thus, the LO3 mode appears to have a significant angular dispersion for $0.4 < \theta < 0.6(\pi/2)$, and so does the LO5 mode for $0.6 < \theta < 1.0(\pi/2)$. So for $0.4 < \theta < 0.6(\pi/2)$, the mode labeled by LO3 has strong LO1 character, and for $0.6 < \theta < 1.0(\pi/2)$, the mode labeled by LO5 has strong LO1 character. Therefore, the definitions of LOn and TON are only meaningful along the k_z direction ($\theta=0$). Similarly, the GaAs-like LO1 mode and LO3 modes interact at θ near $0.5(\pi/2)$. Note that because the superlattice has reflection symmetry about the midplane, modes of even n and modes of odd n cannot mix.

To examine the dependence of angular dispersion of optical modes on the slab thickness, we plot in Fig. 7 the zone-center principal optical phonon frequencies at $\theta=0$ and $\theta=\pi/2$ of $(m,4)$ GaAs-AlAs superlattices as functions of m . We see that the frequency difference $|\nu(\theta=\pi/2) - \nu(\theta=0)|$ for AlAs-like modes increase with m , whereas this quantity for GaAs-like modes decreases with m . The small oscillation in the frequency of the GaAs-like TO mode at $\theta=\pi/2$ as a function of m is due to the interaction of this mode with other modes ($n \neq 1$) of similar frequencies. As m approaches zero (the bulk AlAs limit), the frequency difference for AlAs-like modes goes to zero as expected. As m approaches infinity, the system contains isolated AlAs slabs separated by infinitely thick GaAs slabs. Thus, the frequency difference for GaAs-like modes goes to zero just like in bulk GaAs. On the other hand, the AlAs-like modes should behave like what is expected from the slab model,⁶ which predicts that at $\theta=\pi/2$ the LO mode (x -like) takes on the bulk TO frequency, whereas the TO mode (z -like) takes on the bulk LO frequency. Such a trend is indeed observed in Fig. 7.

To better understand the vibrational behavior of zone-center optical phonons, we need to examine the displacement vectors $U_i(J, \sigma)$. We find that for fixed i and σ ,

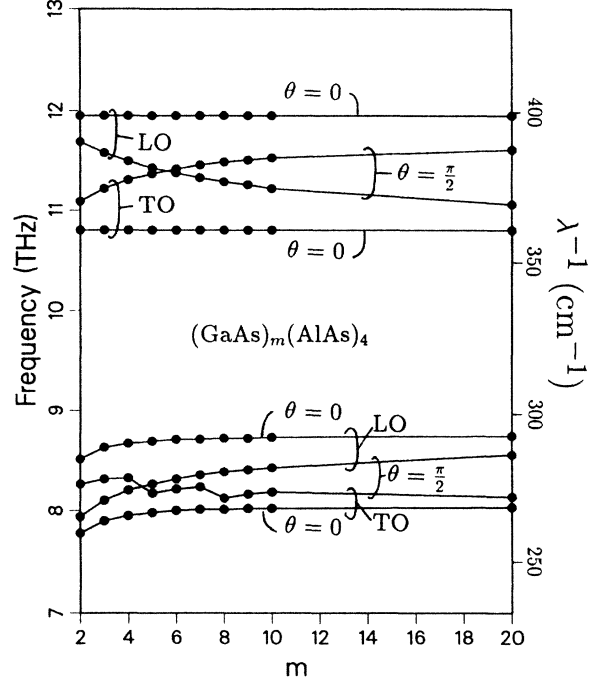


FIG. 7. Frequencies of zone-center principal optical modes at $\theta=0$ and $\theta=\pi/2$ for $(m,4)$ GaAs-AlAs superlattices as functions of m . The upper (lower) set is for AlAs (GaAs)-like modes.

$U_i(J, \sigma)$ can be interpolated by a smooth function. At $\theta=0$ the displacement vector of each mode is either a symmetric (for n odd) or antisymmetric (for n even) function with respect to the midplane, and they can be fit almost perfectly by sine or cosine functions. Figure 8 shows the As-component displacement vectors for a number of GaAs-like zone-center optical modes for the $(7,7)$ GaAs-AlAs superlattice. The corresponding Ga (or Al) component displacement vectors (not shown) have the same shape but with opposite signs. In these two figures, the triangles represent Ga atoms, the squares represent Al atoms, and the black dots represent As atoms. The dotted lines indicate vibrations along x , the solid lines indicate vibrations along y , and the dashed lines indicate vibrations along z . The plots (a)–(g) in the left panel of Fig. 8 are (from top to bottom) for GaAs-like LO1, LO2, LO3, LO4, LO5, and TO1 (doubly degenerated) modes, with \mathbf{k} approaching zero from the z direction (i.e., $\theta=0$), which correspond to the modes with frequencies ranging from 8.7 to 8.0 THz shown at the left side of Fig. 6. Plots (a)–(g) in the right panel of Fig. 8 are for the same set of modes, but with \mathbf{k} approaching zero from the x direction (i.e., $\theta=\pi/2$), which correspond to the modes with frequencies ranging from 8.6 to 8.0 THz at the right side of Fig. 6. The displacement vectors of modes with $\theta=\pi/2$ are different from those with $\theta=0$ in the following ways. First, the ordering in frequency for these modes are different. This is due to the angular dispersion as shown in Fig. 6. Second, stronger mixing of different modes is present at $\theta=\pi/2$. For example, (b)

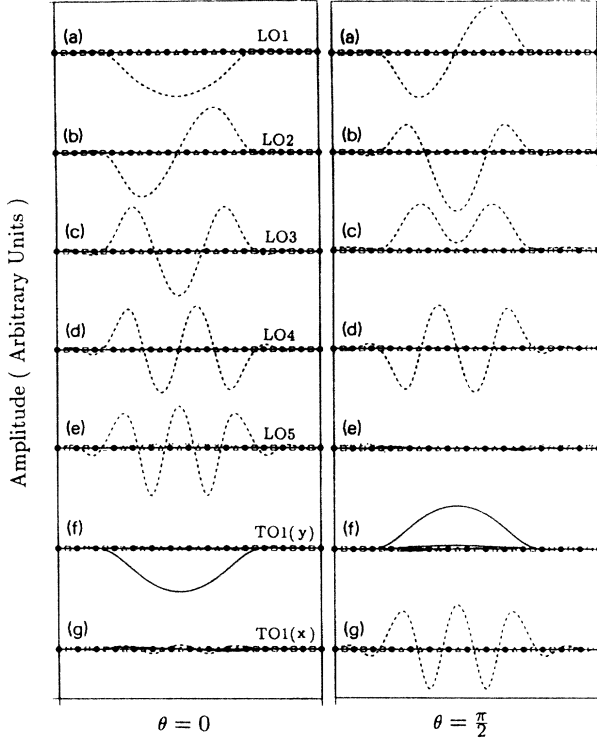


FIG. 8. As-component displacement vectors for a number of GaAs-like zone-center optical modes for the (7,7) GaAs-AlAs superlattice. Left panel, \mathbf{k} approaches zero from the z direction ($\theta=0$); right panel, \mathbf{k} approaches zero from the x direction ($\theta=\pi/2$).

and (c) in the right panel of Fig. 8 show strong mixing of LO1 and LO3. Third, the displacement vectors of some modes at $\theta=\pi/2$ can no longer be interpolated by a sine or cosine function [see (e)].

Figure 8 shows clearly the confinement of GaAs-like optical modes in the GaAs slab. Qualitatively similar results are obtained for AlAs-like optical modes. Due to the confinement of optical phonons in the superlattice, it was suggested that the frequencies of zone-center optical phonons in superlattices can be approximated by the corresponding bulk phonon frequencies $\omega_0(k_n)$. Two ways of determining k_n were previously used.^{9,28} In Ref. 7, $k_n = n\pi/N_s a'$, and in Ref. 28, $k_n = n\pi/(N_s + 1)a'$, where N_s is the number of bilayers within the slab in which the optical mode is confined and a' is the width of a bilayer. This is in analogy to an electron confined by an infinite barrier. However, we find that the choice in between, i.e., $k_n = n\pi/(N_s + \frac{1}{2})a'$, gives the best results (and it also gives the best fitted envelope function of the displacement vectors). This is probably due to the fact that the system has two atomic planes in each bilayer. To test this simple scheme we plot in Fig. 9 the GaAs-like optical phonon frequencies for $\mathbf{k}\rightarrow\mathbf{0}$ along the growth direction with $n=1-4$ of $(m,4)$ GaAs-AlAs superlattices and in Fig. 10 the corresponding AlAs-like optical phonon frequencies for $(4,m)$ GaAs-AlAs superlattices as functions of m . The solid circles in these two figures represent results of the superlattice calculation, and the solid curves are the

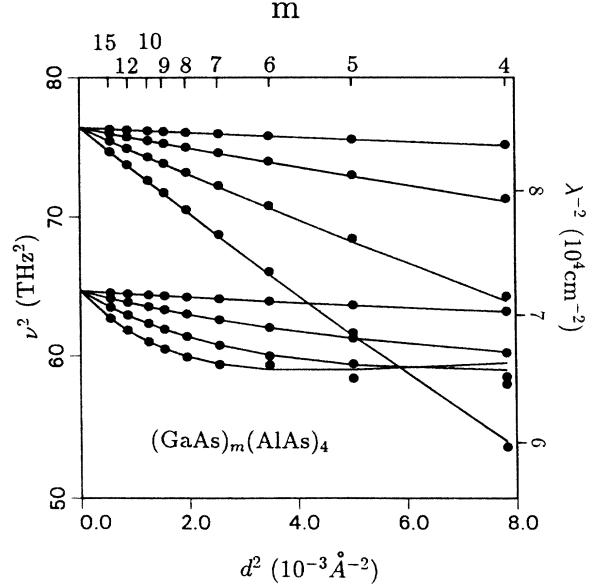


FIG. 9. GaAs-like optical phonon frequencies squared (v^2) for $\mathbf{k}\rightarrow\mathbf{0}$ along the growth direction of $(m,4)$ GaAs-AlAs superlattices as a function of d^2 ; d is the period of the superlattice. Solid circles, present calculation; solid curves, interpolation using bulk GaAs phonon frequencies. The top four curves are for LO ($n=1-4$) modes and the bottom four curves are for TO ($n=1-4$) modes.

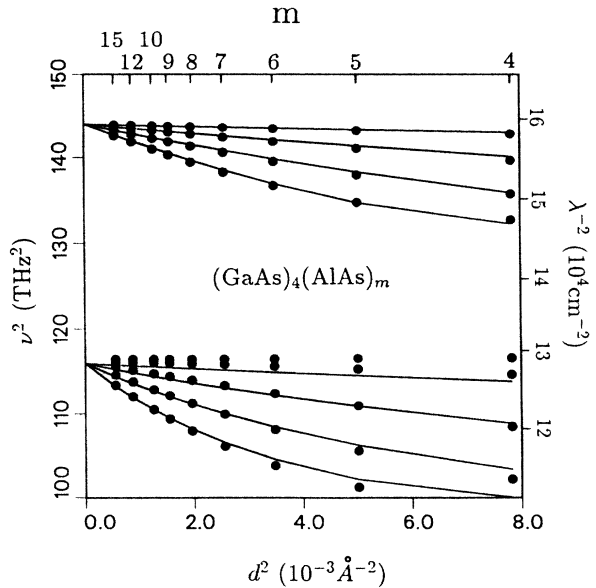


FIG. 10. AlAs-like optical phonon frequencies squared (v^2) for $\mathbf{k}\rightarrow\mathbf{0}$ along the growth direction of $(4,m)$ GaAs-AlAs superlattices as a function of d^2 . Solid circles, present calculation; solid curves, interpolation using bulk AlAs phonon frequencies. The top four curves are for LO ($n=1-4$) modes and the bottom four curves are for TO ($n=1-4$) modes.

predictions of using the bulk phonon frequencies $\omega_0(k_n)$. Note that because of the anisotropy of zone-center optical phonons, we have to specify the direction in which \mathbf{k} approaches zero. We find that the GaAs-like modes and the AlAs-like LO modes are well described by the simple scheme. The AlAs-like TO modes are less well described by the simple scheme, where the first TO mode (nodeless) has a frequency inside the gap of bulk AlAs optical frequencies, so it is an interface mode. This interface mode persists even if we smoothly average out the short-range interaction parameters near the interface. It should be pointed out that the interface modes found here are model dependent. They may not appear, for example, in the shell model or the bond-charge model. However, there exists another type of interface mode which is not model dependent. We shall discuss the details of these interface modes in the next section.

IV. INTERFACE MODES

In general, there exist two types of interface modes in superlattice structures made of polar materials. The first type is caused by the dissimilarity in the short-range interactions of the two constituent bulk materials in the superlattice. Thus, it also exists in superlattices made of nonpolar materials (e.g., the Si-Ge superlattice). Such interface modes can only be obtained in a microscopic model and shall be referred to as “microscopic interface modes.” The second type is caused by the difference in the dynamic dielectric functions of the two constituent materials.^{9–12} In the long-wavelength limit, such interface modes have frequencies which satisfy a transcendental equation identical to that for the principal optical modes with in-plane propagation (i.e., $\theta = \pi/2$) in Rytov’s dielectric continuum model.⁸ These interface modes always exist in polar heterostructures, and we shall refer to them as the “macroscopic interface modes,” since they are caused by the mismatch of macroscopic polarization fields on both sides of the interface.

In our microscopic model with the Coulomb interaction properly included, both types of interface modes can be found. In our calculations, the interface modes can be identified by comparing the superlattice phonon dispersion curves with the bulk phonon dispersion curves. Sood and co-workers⁷ performed resonant Raman scattering experiments on a number of GaAs-AlAs superlattices and observed some macroscopic interface modes. Two of their samples, *A* and *B*, correspond to our (7,7) and (7,21) superlattices. Figures 11 and 12 show the phonon dispersion curves of these two superlattices along [100] (right panel) and [110] (left panel). For comparison, we also plot in Figs. 13 and 14 the projected phonon bands of bulk GaAs and AlAs along the same two directions. The projected phonon bands are obtained by superposing the phonon frequencies for a large number of k_z values for each fixed \mathbf{k}_{\parallel} (the projection of \mathbf{k} in the surface Brillouin zone). By comparing the phonon dispersion curves of the (7,7) and (7,21) GaAs-AlAs superlattices in Figs. 11 and 12 with the projected phonon bands of bulk GaAs (Fig. 13) and AlAs (Fig. 14), we can extract those interface modes which appear in the gaps of the

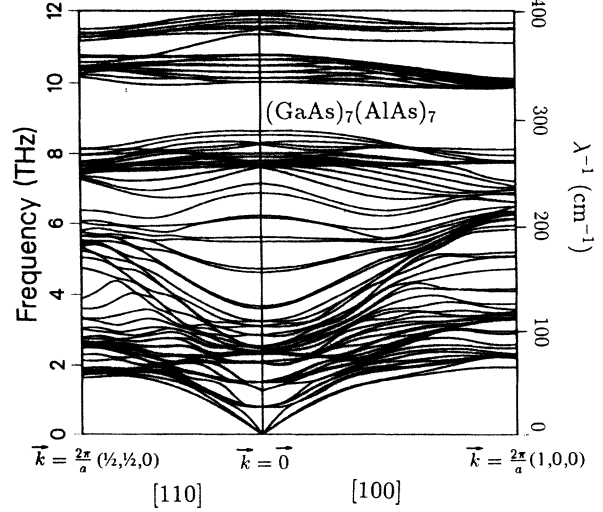


FIG. 11. Dispersion curves of a (7,7) GaAs-AlAs superlattice along [110] and [100].

bulk projected phonon bands. Some of these interface modes penetrate into the bulk modes and turn into resonances which are not easily extractable.

The extracted interface modes for the (7,7) superlattice are shown in Fig. 15. In this figure, the solid curves are macroscopic interface modes and the dashed curves are microscopic interface modes. We found that the interface mode frequencies at large \mathbf{k}_{\parallel} are insensitive to the number of GaAs or AlAs bilayers within each period (N_1 or N_2) as long as both N_1 and N_2 are large (≥ 4). This is due to the strong localization of the interface modes when \mathbf{k}_{\parallel} is large.^{9,10} The GaAs macroscopic interface mode frequencies range from 7.8 to 8.05 THz for \mathbf{k}_{\parallel} from $0.8(2\pi/a)$ to $0.3(2\pi/a)$ and they turn into the principal modes at smaller \mathbf{k}_{\parallel} where their frequencies become

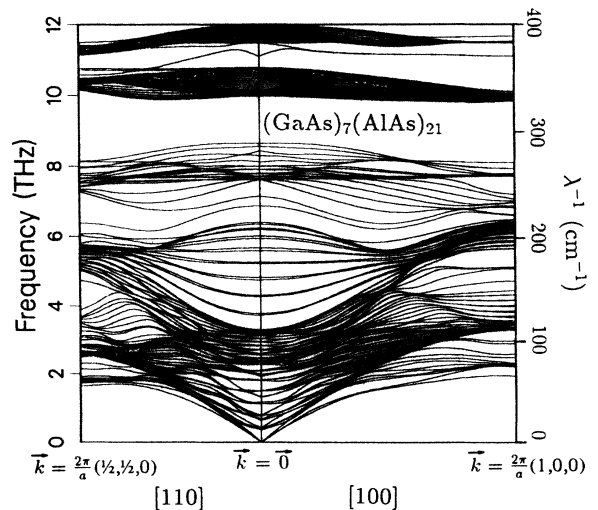


FIG. 12. Dispersion curves of a (7,21) GaAs-AlAs superlattice along [110] and [100].

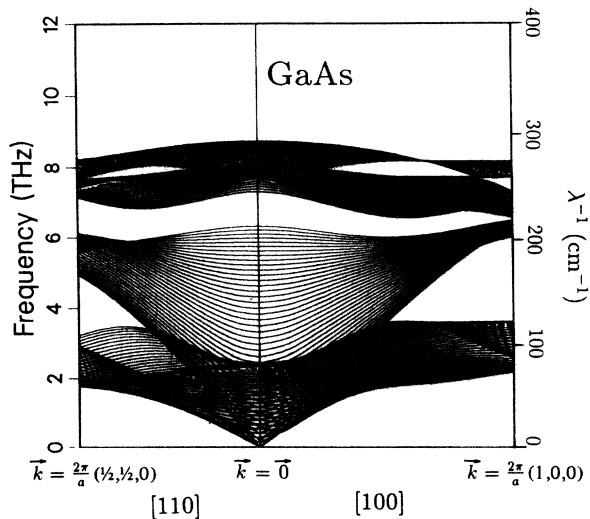


FIG. 13. Projected phonon bands of the bulk of GaAs along [100] and [110].

dependent on N_1 and N_2 . The interface modes observed by Sood *et al.*⁷ in both samples *A* and *B* are peaked around 278 cm^{-1} , which correspond to 268 cm^{-1} or 8.03 THz at room temperature. Thus our theoretical prediction is in accord with the experiment.

To see the connection between the macroscopic interface modes and the in-plane principal optical modes, we plot in Fig. 16 the As-component displacement vectors of the AlAs-like macroscopic interface modes at a number of in-plane wave vectors. In this figure, the modes shown in the left panel have higher frequencies than the corresponding modes shown in the right panel. At $\mathbf{k}_{\parallel} = (0.5, 0)(2\pi/a)$ there are two AlAs-like macroscopic interface modes, one for each of the two interfaces. Their As-component displacement vectors are similar in shape and are almost the mirror image of the complex conju-

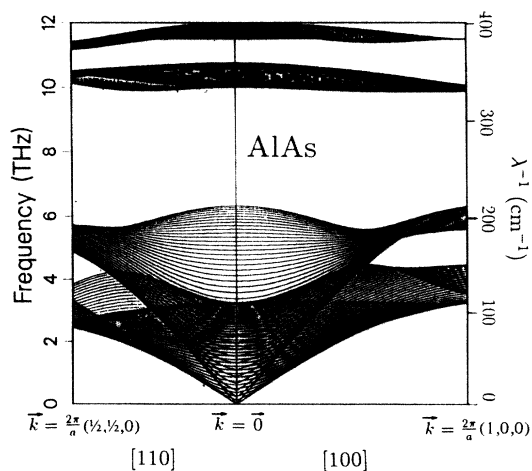


FIG. 14. Projected phonon bands of the bulk of AlAs along [100] and [110].

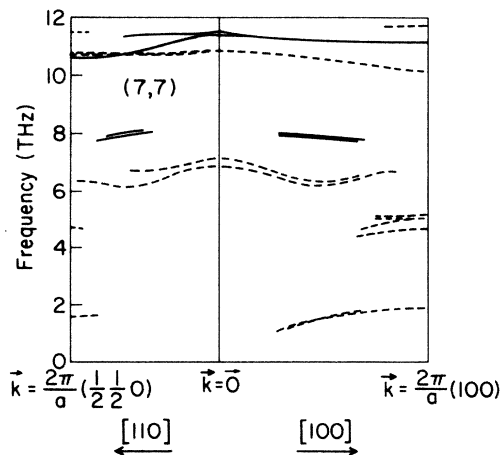


FIG. 15. Dispersion curves of interface modes for the (7,7) GaAs-AlAs superlattice. Solid curves, macroscopic interface modes; dashed curves, microscopic interface modes.

gate of each other [see (e)]. The frequencies of the two interface modes are nearly the same, indicating a very weak interaction between the two. As the magnitude of \mathbf{k}_{\parallel} reduces, the interaction between the two interface modes increases, and we see a larger frequency splitting (see Fig. 15) and the As-component displacement vectors become linear combinations of the two. Near the zone center [e.g., $\mathbf{k}_{\parallel} = (\frac{1}{8}, 0)(2\pi/a)$] the reflection symmetry begins to play a role, and we find the two interface modes behave like bonding (symmetric combination) and antibonding (antisymmetric combination) states of the originally

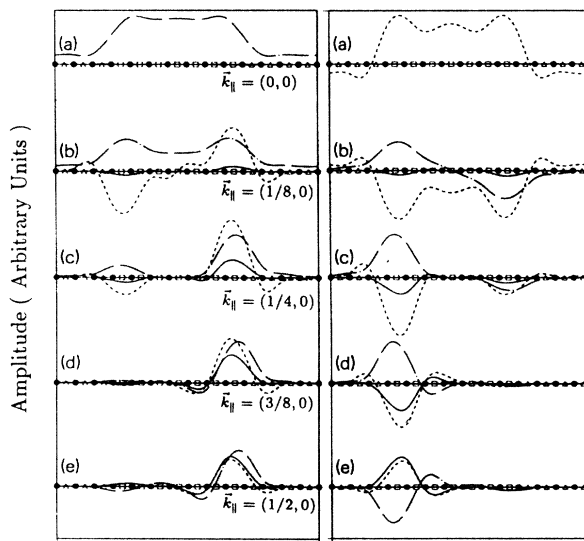


FIG. 16. As-component displacement vectors of the AlAs-like macroscopic interface modes for the (7,7) superlattice at a number of in-plane wave vectors [(a)–(e): from $\mathbf{k} = (0, 0)$ to $\mathbf{k} = (\frac{1}{2}, 0)(2\pi/a)$]. \cdots , $\text{Im}U_x$; — , $\text{Im}U_y$; --- , $\text{Re}U_z$.

decoupled interface modes located at two interfaces. Because the interface modes in general contain both in-plane (e.g., x) and perpendicular (z) components, one of the interface modes contains z -like bonding character and x -like antibonding character, while the other interface mode contains just the opposite. At the zone center ($\mathbf{k}_{\parallel}=\mathbf{0}$ with $\theta=\pi/2$), the antibonding character in both these interface modes are lost, and the two modes turn into the LO1 (x -like) and TO1 (z -like) in-plane modes, respectively. Those antibonding characters are completely absorbed by the LO2 (z -like) and TO2 (x -like) modes. Alternatively we may describe the situation as follows. Start with the LO1 and TO1 modes at $\mathbf{k}_{\parallel}=\mathbf{0}$. The two modes then mix with the LO2 and TO2 modes, respectively, as \mathbf{k}_{\parallel} deviates from zero, and then eventually merge into two nearly degenerate interface modes at large \mathbf{k}_{\parallel} . The fact that the two interface modes couple strongly at smaller \mathbf{k}_{\parallel} is consistent with the macroscopic theory^{9,10} which predicts that the spatial extent of the interface mode is inversely proportional to \mathbf{k}_{\parallel} .

V. SUMMARY

In summary, we have performed calculations on phonon modes in a number of GaAs-AlAs superlattices by using the rigid-ion model. With a proper treatment of the long-range Coulomb interaction, we predicted the anisotropy of zone-center optical modes and the interface modes. All the results compare favorably to the existing experimental data.

Note added. After the completion of this work, a similar work on lattice dynamics in GaAs/AlAs superlattices²⁹ was brought to our attention. In this work, the anisotropy of optical modes and the interface modes were studied in the shell model.

ACKNOWLEDGMENTS

We would like to thank M. V. Klein for fruitful discussions. This work was supported by the U.S. Office of Naval Research (ONR) under Contract No. N00014-81-K-0430 and the University of Illinois Materials Research Laboratory under the National Science Foundation (NSF) Contract NSF-DMR-16981.

APPENDIX: COULOMB MATRIX ELEMENTS

To calculate the dynamic matrix elements for a crystal, we often need to calculate the Bloch sum of an arbitrary potential, V :

$$\phi(\mathbf{k}, \mathbf{r}) = \sum_{\mathbf{l}} V(\mathbf{l} + \mathbf{r}) e^{i\mathbf{k} \cdot \mathbf{l}}, \quad (\text{A1})$$

where \mathbf{l} denotes the lattice vectors and \mathbf{r} denotes an arbitrary position vector within the unit cell. For the long-range Coulomb interaction the summation converges extremely slowly. Rewriting the sum in the reciprocal space, we have

$$\phi(\mathbf{k}, \mathbf{r}) = \frac{1}{v} \sum_{\boldsymbol{\tau}} \tilde{V}(\boldsymbol{\tau} + \mathbf{k}) e^{-i(\boldsymbol{\tau} + \mathbf{k}) \cdot \mathbf{r}}, \quad (\text{A2})$$

where v is the volume of the unit cell, $\boldsymbol{\tau}$ is a reciprocal-

lattice vector, and

$$\tilde{V}(\mathbf{k}) = \int d\mathbf{r} V(\mathbf{r}) e^{i\mathbf{k} \cdot \mathbf{r}}. \quad (\text{A3})$$

Note that the summation has the same form in both real and reciprocal spaces. Thus we can choose whichever form converges faster.

The annoying feature about the Coulomb potential is that neither in real space nor in reciprocal space does the potential decay fast enough to ensure a good convergence. The essence of the Ewald transformation is to break up the potential into two separate terms, one of them (V^S) is slowly varying in real space (thus decaying fast in reciprocal space), while the other (V^F) is fast-decaying in real space: $V(R) = V^S(R) + V^F(R)$. Thus we can write

$$\phi(\mathbf{k}, \mathbf{r}) = \frac{1}{v} \sum_{\boldsymbol{\tau}} \tilde{V}^S(\boldsymbol{\tau} + \mathbf{k}) e^{-i(\boldsymbol{\tau} + \mathbf{k}) \cdot \mathbf{r}} + \sum_{\mathbf{l}} V^F(\mathbf{l} + \mathbf{r}) e^{i\mathbf{k} \cdot \mathbf{l}}. \quad (\text{A4})$$

In general, the choice of V^S and V^F is not unique. The Ewald transformation for Coulomb potential in a bulk system has offered us an excellent example for the choice of V^F and V^S . In Ewald's method,

$$\frac{1}{r} = V^S(r) + V^F(r), \quad (\text{A5})$$

with

$$V^S(r) = \frac{1}{r} \operatorname{erf}(\alpha r) \quad \text{and} \quad V^F(r) = \frac{1}{r} \operatorname{erfc}(\alpha r),$$

where α is an adjustable parameter. The same method can be applied to systems of any dimension.

The Fourier transform of the slowly varying function is

$$\begin{aligned} \tilde{V}^S(k) &= \int d\mathbf{r} V^S(r) e^{i\mathbf{k} \cdot \mathbf{r}} \\ &= 2 \left[\frac{2\sqrt{\pi}}{k} \right]^{d-1} \int_{k/2\alpha}^{\infty} t^{d-2} e^{-t^2} dt \\ &= \left[\frac{2\sqrt{\pi}}{k} \right]^{d-1} \Gamma \left[\frac{d-1}{2}, \frac{k^2}{4\alpha^2} \right], \end{aligned}$$

where d is the dimensionality of the system and $\Gamma(\alpha, x)$ is the incomplete Gamma function

$$\Gamma(\alpha, x) = \int_x^{\infty} e^{-t} t^{\alpha-1} dt.$$

Thus

$$\tilde{V}^S(k) = \begin{cases} \frac{2\pi}{k} \operatorname{erfc}(k/2\alpha) & \text{for 2D systems} \\ \frac{4\pi}{k^2} e^{-k^2/4\alpha^2} & \text{for 3D systems} \end{cases}.$$

For the fast converging function, its second-order derivatives are

$$\begin{aligned} V_{ij}^F(r) &= \frac{3r_i r_j - \delta_{ij} r^2}{r^5} \operatorname{erfc}(\alpha r) \\ &\quad - \frac{2\alpha^3}{\sqrt{\pi}(\alpha r)^2} e^{-(\alpha r)^2} \left[\delta_{ij} - \frac{r_i r_j}{r^2} (2\alpha^2 r^2 + 3) \right]. \end{aligned}$$

We now consider the dynamic matrix elements in a superlattice system. In general, we have

$$\phi_{ij}(\mathbf{k}, \mathbf{r}_{J\sigma}) = -\frac{1}{v} \sum_{\tau} \tilde{V}^S(\tau + \mathbf{k})(\tau + k)_i(\tau + k)_j e^{-i(\tau + \mathbf{k}) \cdot \mathbf{r}_{J\sigma}} + \sum_{l_s} V_{ij}^F(l_s + \mathbf{r}_{J\sigma}) e^{i\mathbf{k} \cdot l_s}, \quad (\text{A6})$$

where $\mathbf{r}_{J\sigma}$ denotes the equilibrium positions of ions in a superlattice unit cell and l_s denotes the superlattice lattice vectors. Here J labels different bulk unit cells within a superlattice unit cell and σ labels atomic positions within each bulk unit cell. Below we shall restrict our discussions to zinc-blende materials. So, $\sigma = 1$ and 2 for cation and anion, and J becomes an index for the positions of bilayers inside a superlattice period. In a superlattice with N bilayers per period, we have $l_s = (l_1, l_2, J + l'N)a/2$ (a is the lattice constant), where l_1 , l_2 , and l' are integers subject to the constraint

$$l_1 + l_2 + J + l'N \text{ even.}$$

$\tau = \tau_{\parallel} + (2\pi m / Na) \hat{z}$, where m is an integer and τ_{\parallel} is a 2D reciprocal lattice vector in the plane perpendicular to the growth direction. Note that when we are dealing with the dynamics of the ions we must avoid the self-interaction term ($l_s = 0$ and $\mathbf{r}_{J\sigma} = 0$), the term with $l_s = 0$ must be excluded in the real-space summation involving V^F , and the term $V^S(0)$ should be subtracted from the \mathbf{k} -space summation involving \tilde{V}^S . When r is small

$$V^S(r) \approx \frac{2\alpha}{\sqrt{\pi}} \left[1 - \frac{\alpha^2 r^2}{3} \right].$$

Hence

$$V_{ij}^S(0) = -\frac{4\alpha^3}{3\sqrt{\pi}} \delta_{ij}.$$

Note that when $\alpha = \sqrt{\pi}$ (in units of $2/a$), $V_{ij}^S(0) = -(4\pi/3)\delta_{ij}$, which is just the local Lorentzian field in a cubic bulk crystal. For small-period superlattices the above equation provides an efficient way for calculating the Coulomb matrix elements. For large-period superlattices it is more advantageous to use the layer method which we will discuss below.

For the discussions that follow, we shall write the wave vector (or reciprocal lattice vector) in units of $(2\pi/a)$ and the lattice vectors in units of $(a/2)$. In the layer method, we first calculate the Coulomb interaction between two

layers of atoms separated by a distance $l_3 + z_{\sigma}$, where z_{σ} is the z component of \mathbf{r}_{σ} ; $\mathbf{r}_{\sigma} = (0, 0, 0)$ and $(1, 1, 1)/2$ for $\sigma = 1$ and 2 , respectively. This is done by performing the summation in (A1) over l_1 and l_2 with l_3 fixed, viz.,

$$\Phi(\mathbf{k}, \mathbf{r}_{\sigma}, l_3) = \sum_{l_1, l_2} \frac{e^{i\mathbf{k} \cdot l}}{[(l_1 + x_{\sigma})^2 + (l_2 + y_{\sigma})^2 + (l_3 + z_{\sigma})^2]^{1/2}} \times [1 + (-1)^{l_1 + l_2 + l_3}], \quad (\text{A7})$$

where $l = (l_1, l_2, l_3)$ denotes the bulk Bravais lattice vectors and $l + \mathbf{r}_{\sigma}$ indicates the position of an atom in layer 2 relative to an atom in layer 1; $\mathbf{r}_{\sigma} = (x_{\sigma}, y_{\sigma}, z_{\sigma})$. The factor $[1 + (-1)^{l_1 + l_2 + l_3}]$ appearing in the summation ensures that the constraint that $l_1 + l_2 + l_3$ must be even is satisfied (for the face-centered cubic lattice). To facilitate the computation of Coulomb matrix elements, we rewrite (A7) in the form

$$\Phi(\mathbf{k}, \mathbf{r}_{\sigma}, l_3) = \Phi_c(\mathbf{k}, \mathbf{r}_{\sigma}, l_3) + \Phi_c(\mathbf{k} - \mathbf{1}, \mathbf{r}_{\sigma}, l_3),$$

where $\mathbf{1} \equiv (1, 1, 1)$ and $\Phi_c(\mathbf{k}, \mathbf{r}_{\sigma}, l_3)$ is given by (A7) with the constraint factor $[1 + (-1)^{l_1 + l_2 + l_3}]$ suppressed.

The Coulomb matrix elements between two atomic layers are defined by

$$\begin{aligned} \bar{C}_{i,j}(\mathbf{r}_{\sigma}, \mathbf{k}, l_3) &= -\left. \frac{\partial^2 \Phi(\mathbf{k}, \mathbf{r}, l_3)}{\partial r_i \partial r_j} \right|_{\mathbf{r}=\mathbf{r}_{\sigma}} \\ &= -S_{i,j}(\mathbf{k}, \mathbf{r}_{\sigma}, l_3) - S_{i,j}(\mathbf{k} - \mathbf{1}, \mathbf{r}_{\sigma}, l_3), \end{aligned}$$

where

$$S_{i,j}(\mathbf{k}, \mathbf{r}_{\sigma}, l_3) \equiv \left. \frac{\partial^2 \Phi_c(\mathbf{k}, \mathbf{r}, l_3)}{\partial r_i \partial r_j} \right|_{\mathbf{r}=\mathbf{r}_{\sigma}}. \quad (\text{A8})$$

In the above expressions, we have set the factor $(Q_1 Q_2 / v)$ equal to unity by choosing proper energy units, where Q_1 and Q_2 are electron transfer charges for atoms in layer 1 and layer 2, respectively.

We shall consider two cases.

(i) *Intralayer interaction* ($l_3 + z_{\sigma} = 0$). In this case, the Coulomb matrix element is independent of k_z ; thus, we can simply use Ewald's method for a two-dimensional (2D) system. We choose $\alpha = \sqrt{\pi}$ (in units of $2/a$) so that the summations of matrix elements in a cubic bulk system are zero except for the irregular term. For the dynamic matrix elements, we have

$$\begin{aligned} S_{i,j}(\mathbf{k}, \rho_{\sigma}, l_3) &= \frac{4\alpha^3}{3\sqrt{\pi}} \delta_{ij} \delta_{\rho_{\sigma}, 0} - \frac{\pi^2}{v} \sum_{\mathbf{n}} V^S(2\mathbf{n} + \mathbf{k})(2\mathbf{n} + k)_i(2\mathbf{n} + k)_j e^{-i\pi(2\mathbf{n} + \mathbf{k}) \cdot \rho_{\sigma}} + \sum_l' V_{ij}^F(l) e^{i\pi l \cdot \mathbf{k}}, \\ &= \frac{4\pi}{3} \delta_{ij} \delta_{\rho_{\sigma}, 0} - \frac{2\pi^2}{v} \sum_{\mathbf{n}} \text{erfc}(\sqrt{\pi} |\mathbf{2n} + \mathbf{k}| / 2) \frac{(2\mathbf{n} + k)_i(2\mathbf{n} + k)_j}{|\mathbf{2n} + \mathbf{k}|} e^{-i\pi(2\mathbf{n} + \mathbf{k}) \cdot \rho_{\sigma}} + \sum_l' H_{ij}(l) e^{i\pi l \cdot \mathbf{k}}, \quad (\text{A9}) \end{aligned}$$

where $\mathbf{n}=(n_1, n_2)$, $\rho_\sigma=(x_\sigma, y_\sigma)$, and

$$H_{ij}(\mathbf{r}) \equiv \frac{3r_i r_j - \delta_{ij} r^2}{r^5} \operatorname{erfc}(\sqrt{\pi} r) - \frac{2}{r^2} e^{-\pi r^2} \left[\delta_{ij} - \frac{r_i r_j}{r^2} (2\pi r^2 + 3) \right].$$

The symbol \sum' indicates that the $l=0$ term is to be excluded.

(ii) *Interlayer interaction* ($l_3 + z_\sigma \neq 0$). In this case, the two-dimensional potential is itself a slowly varying function in real space. The Fourier transform of the potential is an exponentially decaying function in the 2D \mathbf{k} space, viz.,

$$\bar{V}(k) = \int d\rho \frac{e^{i\mathbf{k}\cdot\rho}}{[\rho^2 + (l_3 + z_\sigma)^2]^{1/2}} = 2 \frac{e^{-\pi k |l_3 + z_\sigma|}}{k}. \quad (\text{A10})$$

Thus we have

$$S_{i,j}(\mathbf{k}, \mathbf{r}_\sigma, l_3) = -2\pi^2 \sum_{\mathbf{n}} \frac{K_i K_j}{K} f_{n,l_3}(\mathbf{r}_\sigma, \mathbf{k}), \quad (\text{A11})$$

$$S_{i,z}(\mathbf{k}, \mathbf{r}, l_3) = -i2\pi^2 \sum_{\mathbf{n}} K_i \frac{l_3 + z_\sigma}{|l_3 + z_\sigma|} f_{n,l_3}(\mathbf{r}_\sigma, \mathbf{k}), \quad (\text{A12})$$

$$S_{z,z} = -S_{x,x} - S_{y,y},$$

where $\mathbf{K}=(2n_1 + k_x, 2n_2 + k_y)$, $\mathbf{n}=(n_1, n_2)$, $i, j = x, y$, and

$$f_{n,l_3}(\mathbf{r}_\sigma, \mathbf{k}) = e^{-\pi K |l_3 + z_\sigma| - i\pi \mathbf{K} \cdot \rho_\sigma + i\pi k_z l_3}.$$

Next we sum over the interlayer matrix elements over l_3 . To get the Coulomb interaction between two different sublattices separated by $J + z_\sigma$, we factor out the terms involving l_3 in the above equations and carry out the sum over l_3 separately in closed forms. This summation can be done by replacing l_3 by $l'N + J$ ($J=0, \dots, N-1$) and summing over all integers l' . We obtain

$$\sum_{l'} f_{n,l'N+J}(\mathbf{r}_\sigma, \mathbf{k}) = \left[\frac{e^{-(J+z_\sigma)K^-}}{1 - e^{-NK^-}} \pm \frac{e^{-(N-J-z_\sigma)K^+}}{1 - e^{-NK^+}} \right] \times e^{-i\pi \mathbf{K} \cdot \rho_\sigma - i\pi k_z z_\sigma},$$

where $K^\pm = \pi(K \pm ik_z)$. The “+” sign is for $\bar{C}_{x,x}$ and $\bar{C}_{y,y}$, and the “-” sign is for $\bar{C}_{x,z}$. For $\mathbf{r}_\sigma=0$ and $J=0$ we shall exclude the $l'=0$ term, which is treated separately according to procedures given in category (i), and we have

$$\sum_{l'(\neq 0)} f_{n,l'N}(\mathbf{0}, \mathbf{k}) = \frac{1}{e^{NK^-} - 1} \pm \frac{1}{e^{NK^+} - 1}.$$

Finally, we derive an expression for the Coulomb interaction between a sublattice at the origin and a sublattice at (J, σ) [denoted $C_{i,j}(\mathbf{k}, J, \mathbf{r}_\sigma)$] in the limit $\mathbf{k} \rightarrow 0$. We note that the Coulomb interaction is an irregular function of \mathbf{k} as $\mathbf{k} \rightarrow 0$. Separating out this term with the rest we have

$$C_{i,j}(\mathbf{k}, J, \mathbf{r}_\sigma) = \frac{4\pi}{N} \frac{k_i k_j}{k^2} + D_{i,j}(J, \mathbf{r}_\sigma).$$

The irregular term $(4\pi/N)k_i k_j / k^2$ gives different values as $\mathbf{k} \rightarrow 0$ from different directions. In general, $D_{i,j}(J, \mathbf{r}_\sigma)$ has to be calculated numerically through the equations given above. It should be pointed out that the irregular term is independent of the distance between the two sublattices. Thus any truncation of the Coulomb interaction in the z direction will lead to erroneous results for \mathbf{k} pointing at a direction different from z . For \mathbf{k} along z , however, the truncation is still valid, as the Coulomb interaction between layers falls off quickly as the interlayer distance increases. This can be seen from Eqs. (A11) and (A12) for $k_x = k_y = 0$ with $n_1 = n_2 = 0$.

For a bulk system ($N=1$), $C_{i,j}$ will be reduced to

$$C_{i,j}^0 = 4\pi \left[\frac{k_i k_j}{k^2} - \frac{1}{3} \delta_{i,j} \right],$$

which is exactly the sum of the long-range dipole field and the short-range local field contributions. We thus have

$$\sum_J D_{i,j}(J, \mathbf{r}_\sigma) = -\frac{4\pi}{3} \delta_{i,j}.$$

¹M. V. Klein, IEEE J. Quantum Electron. **QE-22**, 1760 (1986).

²R. Merlin, C. Colvard, M. V. Klein, H. Morkoç, A. Y. Cho, and A. C. Gossard, Appl. Phys. Lett. **36**, 43 (1980).

³C. Colvard, R. Merlin, M. V. Klein, and A. C. Gossard, Phys. Rev. Lett. **45**, 298 (1980).

⁴J. L. Merz, A. S. Barker, Jr., and A. C. Gossard, Appl. Phys. Lett. **31**, 117 (1977).

⁵A. S. Barker, Jr., J. L. Merz, and A. C. Gossard, Phys. Rev. B **17**, 3181 (1978).

⁶J. E. Zucker, A. Pinczuk, D. S. Chemla, A. Gossard, and W. Wiegmann, Phys. Rev. Lett. **53**, 1280 (1984).

⁷A. K. Sood, J. Menedez, M. Cardona, and K. Ploog, Phys. Rev. Lett. **54**, 2111 (1985); **54**, 2115 (1985).

⁸S. M. Rytov, Zh. Eksp. Teor. Fiz. **29**, 605 (1955) [Sov.

Phys.—JETP **2**, 466 (1956)].

⁹E. P. Fuchs and K. L. Kliewer, Phys. Rev. **140**, A2076 (1965).

¹⁰E. P. Pokatilov and S. I. Beril, Phys. Status B **118**, 567 (1983).

¹¹M. Babiker, J. Phys. C **19**, 683 (1986); Physica B + C **145B**, 111 (1987).

¹²L. Wendler, Phys. Status Solidi B **129**, 513 (1985).

¹³S. K. Yip and Y. C. Chang, Phys. Rev. B **30**, 7037 (1984).

¹⁴A. Kobayashi, Ph.D thesis, Department of Physics, University of Illinois at Urbana-Champaign, 1985.

¹⁵T. Toriyama, N. Kobayashi, and Y. Horikoshi, Jpn. J. Appl. Phys. **25**, 1895 (1987).

¹⁶K. Kunc, Ann. Phys. (France) **8**, 319 (1973-1974).

¹⁷K. Kunc, M. Balkanski, and M. Nusimovici, Phys. Status Solidi B **72**, 229 (1975).

- ¹⁸S.-F. Ren, H.-Y. Chu, and Y.-C. Chang, *Phys. Rev. Lett.* **50**, 1841 (1987).
- ¹⁹See, for example, M. Born and K. Huang, *Dynamical Theory of Crystal Lattices* (Oxford University Press, Oxford, 1956).
- ²⁰M. Ilegems and G. L. Pearson, *Phys. Rev. B* **1**, 1576 (1970).
- ²¹A. A. Maradudin, E. W. Montroll, G. H. Weiss, and I. P. Ipatova, *Theory of Lattice Dynamics in the Harmonic Approximation*, 2nd ed., Suppl. 3 of *Solid State Physics*, edited by F. Seitz, D. Turnbull, and H. Ehrenreich (Academic, New York, 1971).
- ²²G. Venkataraman, L. A. Feldkamp, and V. C. Sahni, *Dynamics of Perfect Crystals* (MIT Press, England, 1975).
- ²³J. P. Mathieu and L. Couture-Mathieu, *J. Phys. Radium* **13**, 271 (1952).
- ²⁴C. A. Arguello, D. L. Rousseau, and S. P. Porto, *Phys. Rev.* **181**, 1351 (1969).
- ²⁵W. Hayes and R. London, *Scattering of Light by Crystals* (Wiley, New York, 1978).
- ²⁶D. C. Hurley, S. Tamura, and J. P. Wolfe, *Phys. Rev. Lett.* **58**, 2446 (1987).
- ²⁷S. Tamura, and J. P. Wolfe, *Phys. Rev. B* **35**, 2528 (1987).
- ²⁸B. Jusserand and D. Paquet, *Phys. Rev. Lett.* **56**, 1752 (1986).
- ²⁹E. Richter, Ph.D. thesis, University of Regensburg, 1987 (in German). This work was brought to our attention by M. V. Klein.